Local circuits of layer Vb-to-Va neurons mediate hippocampal-cortical outputs in lateral but not in medial entorhinal cortex

Shinya Ohara[1,§*], Stefan Blankvoort [1], Rajeevkumar R. Nair[1], Maximiliano J. Nigro[1], Eirik S. Nilssen[1], Clifford Kentros[1], Menno P. Witter[1*]

[1]Kavli institute for Systems Neuroscience, Center for Computational Neuroscience, Egil and Pauline Braathen and Fred Kavli Center for Cortical Microcircuits, NTNU Norwegian University of Science and Technology, Trondheim, Norway.
[§]Currently at Laboratory of Systems Neuroscience, Tohoku University Graduate School of Life Sciences, Japan.

* Correspondence:

Menno Witter
Kavli Institute for Systems Neuroscience
Faculty for Medical and Health Sciences, NTNU
Postboks 8905
7491 Trondheim
Norway
Email: menno.witter@ntnu.no

Shinya Ohara
Laboratory of Systems Neuroscience
Tohoku University Graduate School of Life Sciences
Sendai
Japan
shinyaohara@gmail.com

Running title: Only lateral entorhinal cortex layer V neurons mediate hippocampal-cortical output

Word count main text: 4798 words
Word count abstract: 147 words
Number of figures: 6
Supplementary figures: 11

Keywords

parahippocampal region, local circuit, hippocampal-cortical output circuit, hippocampal-entorhinal re-entry circuit, systems memory consolidation

Summary

The entorhinal cortex, in particular neurons in layer V, allegedly mediate transfer of information between the hippocampus and the neocortex, underlying long-term memory. Recently, this circuit has been shown to comprise a hippocampal output recipient layer Vb and a cortical projecting layer Va. With the use of *in vitro* electrophysiology in transgenic mice specific for layer Vb, we assessed the presence of the thus necessary connection between layer Vb and layer Va in the two functionally distinct medial (MEC) and lateral (LEC) subdivisions; MEC processes allocentric spatial information, whereas LEC represents the content of episodes. Using identical experimental approaches, we show that in LEC, but not in MEC, layer Vb neurons provide substantial direct input to layer Va neurons. This indicates that the hippocampal-cortex output circuit is present only in LEC, suggesting that episodic systems consolidation predominantly uses LEC-derived information and not allocentric spatial information from MEC.

Introduction

Everyday memories, which include information of place, time, and content of episodes, gradually mature from an initially labile state to a more stable and long-lasting state. This memory maturation process, called memory consolidation, involves gradual reorganization of interconnected brain regions: memories that are initially depending on hippocampus become increasingly dependent on cortical networks over time (Frankland and Bontempi, 2005). Although various models have been hypothesized for this systems level consolidation, such as the standard consolidation model and multiple trace theory (Nadel and Moscovitch, 1997; Squire and Alvarez, 1995), they all share a canonical hippocampal-cortical output circuit via the entorhinal cortex (EC), which is crucial to mediate long-term memory storage and recall (Buzsáki, 1996; Eichenbaum et al., 2012). The existence of this circuit was originally proposed based on the ground-breaking report of a non-fornical hippocampal-cortical output route mediated by layer V (LV) of the EC in monkeys (Rosene and Van Hoesen, 1977), which was later confirmed also in rodents (Köhler, 1985; Kosel et al., 1982).

The EC is composed of two functionally distinct subdivisions, the lateral and medial EC (LEC and MEC respectively). MEC processes allocentric, mainly spatial information, whereas LEC represents the time and content of episodes (Deshmukh and Knierim, 2011; Hafting et al., 2005; Montchal et al., 2019; Tsao et al., 2018, 2013; Xu and Wilson, 2012). In spite of these evident functional differences, both subdivisions are assumed to share the same cortical output system mediated by LV neurons. Recently we and others have shown that LV in both MEC and LEC can be genetically and connectionally divided into two sublayers: a deep layer Vb (LVb) which contains neurons receiving projections from the hippocampus, and a superficial layer Va (LVa) which originates the main projections out to forebrain cortical and subcortical structures (Ohara et al., 2018; Sürmeli et al., 2015). These results indicate that in order for the hippocampal-cortical dialogue to function, we need to postulate a projection from LVb to LVa neurons. Although the existence of this LVb-LVa circuit is supported by our previous study using transsynaptic viral tracing in rats (Ohara et al., 2018), experimental evidence for functional connectivity from LVb-to-Va in LEC and MEC is still lacking.

In the present study we examined the presence of this hypothetical intrinsic EC circuit by using newly generated LVb-specific transgenic (TG) mice obtained with enhancer-driven gene expression (EDGE) approach (Blankvoort et al., 2018). To compare the LVb intrinsic circuit between LEC and MEC, we ran identical *in vitro* electrophysiological and optogentical experiments in comparable dorsal portions of LEC and MEC. To our surprise, our data do not support the existence of the postulated intrinsic LVb-LVa pathway in the dorsal parts of MEC. However, the connectivity of the dorsal LEC is in line with the proposed circuitry. In contrast, other intrinsic circuits from LVb to layers II and III (LII and LIII), which constitute the hippocampal-entorhinal re-entry circuits, are very similar in both entorhinal subdivisions. These results suggest that the allocentric navigation system lacks the canonical hippocampal-cortical output circuit that allegedly is crucial for systems consolidation. Our data thus point to an important deviation from the current view of how the hippocampus interacts with the neocortex and thus impacts on current theories about systems consolidation and the hippocampal memory system.

Results

Characterization of LVb transgenic mouse line

Entorhinal LV can be divided into superficial LVa and deep LVb based on differences in cytoarchitectonics, connectivity and genetic markers such as purkinje cell protein 4 (PCP4) and chicken ovalbumin upstream promoter transcription factor interacting protein 2 (Ctip2) (Ohara et al., 2018; Sürmeli et al., 2015) (Supplementary Fig.1., see Methods for details). To target the entorhinal LVb neurons, we used a TG mouse line (MEC-13-53D) which was obtained with the EDGE approach (Blankvoort et al., 2018). In this TG line, the tetracycline-controlled transactivator (tTA, Tet-Off) is expressed under the control of a specific enhancer and a downstream minimal promoter. To visualize the expression patterns of tTA, this line was crossed to tTA-dependent reporter mouse which express mCherry together with the tTA dependent GCaMP6.

In both LEC and MEC, mCherry-positive neurons were observed mainly in LVb and sparsely in layer VI (LVI) but not in other layers (Fig. 1A-C). The proportion of PCP4-positive LVb neurons which show tTA-driven labelling was 45.9% in LEC and 30.9% in MEC (Fig. 1D). The tTA-driven labelling colocalized well with the PCP4-labeling (percentage of tTA-expressing neurons that were PCP4-positive was 91.7% in LEC and 99.3% in MEC; Fig. 1E), highlighting the specificity of the line. In another experiment using a GAD67 transgenic line expressing green fluorescent protein (GFP), we showed that the percentage of double-labelled (PCP4+, GAD67+) neurons among total GAD67-positive neurons is very low in both LEC and MEC (4.3% and 2.3% respectively, Supplementary Fig. 2). This percentage of double-labelled neurons was significantly lower than in the Ctip2-stained sample in both regions (18.1% for LEC and 7.2% for MEC). This result shows that PCP4 can be used as a marker for excitatory entorhinal LVb neurons. Taken together with the above results, we concluded that MEC-13-53D is an exquisite TG mouse line to selectively target excitatory LVb neurons in both LEC and MEC.

Morphological properties of LVa/LVb neurons in LEC and MEC

We next examined the morphological and electrophysiological properties of the LVb neurons in LEC and MEC in this TG-mouse line. Targeted LVb neurons were labelled by injecting tTA-dependent adeno-associated virus (AAV) encoding GFP (AAV2/1-TRE-Tight-GFP) into either LEC or MEC and filled with biocytin during whole-cell patch-clamp recordings in

acute slices (Fig. 1F). Consistent with our histological result showing that this line targets excitatory cells, all recorded cells showed morphological and electrophysiological properties of excitatory neurons (Fig. 1, Fig. 2). In line with previous studies, many MEC-LVb neurons were pyramidal cells with apical dendrites that ascended straight towards layer I (LI; Fig. 1G, I) (Canto and Witter, 2012a; Hamam et al., 2000). In contrast, more than 40% of the targeted LEC-LVb neurons were tilted pyramidal neurons (Canto and Witter, 2012b; Hamam et al., 2002) with apical dendrites not extending superficially beyond LIII (Fig. 1H, I). Since this latter result may result from severing of dendrites by the slicing procedure, we also examined the distribution of LVb apical dendrites *in vivo*. After injecting AAV2/1-TRE-Tight-GFP in the deep layer of LEC in the TG line, the distribution of labelled dendrites of LEC-LVb neurons were examined throughout all sections (Supplementary Fig. 3). Even with this approach, the labelled dendrites mainly terminated in LIII and only sparsely reached layer IIb. These morphological differences indicate that MEC-LVb neurons sample inputs from different layers than LEC-LVb neurons: MEC-LVb neurons receive inputs throughout all layers, whereas LEC-LVb neurons only receive inputs innervating layer IIb–VI. In contrast to LVb neurons, the morphology of LVa neurons was relatively similar in both regions: the basal dendrites extended horizontally mostly within LVa whereas the apical dendrites reached LI (Supplementary Fig. 4). These morphological features of LVa neurons are in line with previous studies (Canto and Witter, 2012a, 2012b; Hamam et al., 2000, 2002; Sürmeli et al., 2015).

Electrophysiological properties of LVa/LVb neurons in LEC and MEC

Previous studies have reported that the electrophysiological profiles of LV neurons are diverse both in LEC and MEC (Canto and Witter, 2012a, 2012b; Hamam et al., 2000, 2002), but whether these different electrophysiological properties of entorhinal LV neurons relate to the two sublayers, LVa and LVb, was unclear. Here, we examined this by analysing a total of 121 neurons recorded from the TG mouse line (MEC-13-53D): 31 LEC-LVa, 45 LEC-LVb, 20 MEC-LVa, and 25 MEC-LVb neurons (Fig. 2A). As previously reported (Canto and Witter, 2012a, 2012b; Hamam et al., 2000, 2002), some LV neurons showed a depolarizing afterpotential (DAP; Fig. 2B). The percentage of neurons which showed DAP was higher in MEC LVb (36.0 %) than in LEC-LVa (9.7 %), LEC-LVb (2.2 %), and in MEC-LVa (0 %; Fig. 2F). Among the twelve examined electrophysiological properties (Supplementary Table 1), differences were observed between the LVa and LVb neurons in most parameters except for resting potential, input resistance and action potential (AP) threshold (Fig. 2I-K, Supplementary Fig. 5). Principal component analysis based on the twelve parameters resulted in a clear separation between LVa and LVb neurons, and also in a moderate separation between LEC-LVb and MEC-LVb (Fig. 2L). Sag ratio (Fig. 2C, H), time constant (Fig. 2K), and AP frequency after 200 pA injection (Fig. 2E, J) were the three prominent parameters which separated LVa and LVb neurons (Fig. 2M). The clearest features aiding in separating LEC-LVb and MEC-LVb were time constant (Fig. 2K), AP frequency after 200 pA injection (Fig. 2E, J), and fast afterhyperpolarization (AHP; Fig. 2N, Supplementary Fig. 5). Neurons in MEC-LVb showed a smaller time constant, higher AP frequency, and smaller fast AHP than LEC-LVb neurons. It is of interest that LVb neurons in LEC and MEC differed not only with respect to some of their electrophysiological characteristics, but also morphologically (described above; Fig. 1F-I). Whether these two sets of features are related needs to be determined.

Local projections of LVb neurons in LEC and MEC are different

Subsequently, we examined the local entorhinal LVb circuits, by injecting a tTA-dependent AAV carrying both the channelrhodopsin variant oChiEF and the yellow fluorescent protein

(citrine, AAV2/1-TRE-Tight-oChIEF-citrine) into the deep layers of either LEC or MEC in mouse line MEC-13-53D (Fig. 3A). This enabled specific expression of the fused oChIEF-citrine protein in either LEC-LVb (Fig. 3B-F) or MEC-LVb (Fig. 3G-K). Not only the dendrites and the soma but also the axons of these LVb neurons were clearly labelled. As shown in the horizontal sections taken at different dorsoventral level (Fig. 3B-D, G-I), citrine-labelled axons were observed mainly within the entorhinal cortex, and only very sparse labelling was observed in other regions, including the angular bundle, a major efferent pathway of EC. This result supports our previous study (Ohara et al., 2018) showing that the main targets of the entorhinal LVb neurons are neurons in superficially positioned layers. Within EC, the distribution of labelled axons differed between LEC and MEC (Fig. 3L). Although in both LEC and MEC, labelled axons were densely present in LIII rather than in layers II and I, we report a striking difference between LEC and MEC in LVa, as is easily appreciated from Figure 3L: many labelled axons of LEC-LVb neurons were present in LVa, whereas in case of MEC-LVb, the number of labelled axons was very low in LVa. Based on these anatomical observations, we predicted that LVb neurons in both LEC and MEC innervate LIII neurons rather than LII neurons. Importantly, our findings further indicate that LVb-LVa connections, which mediate the hippocampal-cortical output circuit are much more prominent in LEC than in MEC. To test these predicted connectivity patterns, we used optogenetic stimulation of the oChIEF-labelled axons together with patch-clamp recordings of neurons in the different layers of EC.

Translaminar local connections of MEC-LVb neurons

We first examined the LVb circuits in MEC, by performing patch-clamp recording from principal neurons in layers II (n=20 for stellate cells, n=18 for pyramidal cells), III (n=30), and Va (n=18), while optically stimulating LVb fibers in acute horizontal entorhinal slices (Fig. 4, Supplementary Fig. 6). Recorded neurons were labelled with biocytin, and the neurons were subsequently defined from the location of their cell bodies, morphological characteristics, and electrophysiological properties. In line with previous studies, LIII principal neurons were pyramidal cells, while neurons in LII were either stellate cells or pyramidal neurons (Fig. 4A) (Canto and Witter, 2012a; Fuchs et al., 2016; Winterer et al., 2017). LII stellate cells were not only identified by the morphological features but also from their unique physiological properties, characterized by the pronounced sag potential and DAP (Fig. 4B) (Alonso and Klink, 1993).

There was a densely labelled axonal plexus in LIII, which is the layer where LIII pyramidal neurons mainly distribute their basal dendrites. In line with this anatomical observation, all LIII neurons (30 out of 30 cells) responded to the optical stimulation (Fig. 4C, D). In contrast, the axonal labelling was sparse in LII, and this distribution was reflected in the observed sparser connectivity. The percentage of pyramidal neurons in LII responding to optical stimulation was 61.1% (11 out of 18 cells) and this percentage was especially low in stellate cells (25.0 %; 5 out of 20 cells). Even in the five stellate cells that responded to the light stimulation, evoked responses were relatively small as measured by the amplitude of the synaptic event (Fig. 4C, E, Supplementary Fig. 6). In order to compare the differences of excitatory postsynaptic potential (EPSP) amplitudes across different layers/cell types, the voltage responses of each neuron were normalized to the response of LIII cells recorded in the same slice (Fig. 4F). The normalized EPSP amplitude of LII cells were significantly smaller than those of LIII pyramidal cells, and within LII cells, the responses of stellate cells were significantly smaller than those of pyramidal cells ($p < 0.001$ for LIIs vs LIII and LIIp vs LIII, $p < 0.01$ for LIIs vs LIIp, One-way ANOVA followed by Bonferroni's multiple comparison test). The difference of responses between LII and III neurons are likely due to

the difference of the LVb fiber distribution within these layers. In contrast, the difference of responses between the two cell types in LII might be explained by the difference of the input resistance between these neurons, the input resistances of stellate cells being significantly lower than that of pyramidal cells ($p < 0.001$, One-way ANOVA followed by Bonferroni's multiple comparison test; Fig. 4G), although we cannot exclude the possible difference in total synaptic input between the stellate and pyramidal neurons in LII.

As shown in Supplementary Fig. 4, and also in line with previous studies (Canto and Witter, 2012a; Hamam et al., 2000; Sürmeli et al., 2015), LVa pyramidal cells have their basal dendrites mainly confined to LVa, which is the layer that MEC-LVb neurons avoid to project to (Fig. 3L, Fig. 4A, Supplementary Fig. 6). In line with this anatomical observation, only 27.8% (5 out of 18 cells) responded to the light stimulation (Fig. 4D). The EPSP amplitudes of the responding LVa neurons were relatively small (Fig. 4C, E, Supplementary Fig. 6), and the normalized EPSPs were significantly smaller than those of LIII neurons ($p < 0.001$, One-way ANOVA followed by Bonferroni's multiple comparison test; Fig. 4F). We recorded responses in slices taken at different dorsoventral levels. Since functional differences along this axis has been reported (Steffenach et al., 2005; Stensola et al., 2012), we examined whether the LVb-LVa connectivity differs along the dorsoventral axis, by grouping the recorded LVa responses in three distinct dorsoventral level (Supplementary Fig.7). The voltage responses of the more ventrally positioned LVa neurons were significantly higher than those measured more dorsally in MEC ($p < 0.01$, One-way ANOVA followed by Bonferroni's multiple comparison test). Since the EPSP amplitudes of LIII neurons did not differ at different dorsoventral levels, it is unlikely that the observed response differences are caused by different levels of oChiEF-expression in LVb fibers along the dorsoventral axis.

Although we mainly focused on the projections of LVb neurons to principal neurons in the more superficial layers, a previous electron microscopical study has shown that in MEC 44% of the excitatory deep-to-superficial projections make synapses on non-spiny dendritic shafts, indicative for interneurons as postsynaptic partners (van Haeften et al., 2003). Indeed, all of the putative interneurons that were recorded in superficial MEC showed large voltage response to light stimulation (n=4, Supplementary Fig. 8). In order to examine the potential for disynatic inhibitory inputs from LVb neurons to principal neurons in layer II/III/Va, we recorded the response in principal neurons to light stimulation in voltage-clamp mode holding the membrane potential at either -55 mV or 0 mV. Compared to the current response at -70 mV, the halfwidth of the inward current was smaller at -55 mV, and outward current emerged right after the inward current, which likely reflects the disynaptic inhibitory inputs. The outward current was more obvious at 0 mV without much contribution from excitatory inputs, and in both recording condition, the disynaptic inhibitory inputs were prominent in LIII.

Translaminar local connections of LEC-LVb neurons

We next examined the LVb local circuits in LEC with the similar method as applied in MEC (above). In LEC, LII can further be divided into two sublayers: layer IIa (LIIa) composed of fan cells, and layer IIb (LIIb) mainly composed of pyramidal neurons (Leitner et al., 2016). Fan cells mainly extend their apical dendrites in LI, where the density of LVb labelled-fibers is extremely low (Fig. 5A, Supplementary Fig. 9). This is in contrast to LIIb, LIII, and LVa neurons, which distribute at least part of their dendrites in layers with a relatively high density of LVb axons. In line with this anatomical observation, only 26.9 % of the fan cells (7 out of 26 neurons) responded to the light stimulation (Fig. 5C, D). On the other hand, the response probabilities of LIIb, III, and Va were high, 76.9 % (20 out of 26 cells), 100 % (34 out of 34 cells), and 94.7 % (18 out of 19 cells), respectively. The voltage responses of these neurons were also significantly larger than those of the LIIa neurons ($p < 0.001$, One-way

ANOVA followed by Bonferroni's multiple comparison test; Fig. 5E, F). In contrast to MEC-LII stellate cells, the input resistance of LIIa fan cells was significantly higher than that of LIIb and LIII neurons (Fig. 5G). This indicates that the small responses of LIIa fan cells cannot be explained by the differences in input resistance among the superficial neurons and may simply be due to the small number of synaptic inputs to LIIa fan cells from LVb neurons. In contrast to MEC, LEC-LVa neurons showed large responses to light stimulation, which matched with the anatomically dense LVb fiber distribution in LEC-LVa (Fig. 3L). This striking difference between MEC and LEC regarding LVb to LVa projections is clear from comparing the proportion of responding neurons (Fig. 5H), and the normalized EPSP based on LIII response (Fig. 5I) between MEC and LEC. In contrast to the similar responses of LII neurons between the two subregions, the voltage responses of LEC-LVa neurons were significantly higher than those of MEC-LVa neurons ($p < 0.05$, two-tailed unpaired t-test; Fig. 5I).

We also examined whether LEC LVb neurons exert an inhibitory effect on local excitatory neurons through inhibitory interneurons (Supplementary Fig. 10). The response to light stimulation was recorded in voltage-clamp mode holding the membrane potential at either -55 mV or 0 mV. Prominent disynaptic inhibitory inputs were observed in LIII and Va neurons, whereas the percentage of neurons receiving disynaptic inhibitory inputs was low in LIIa neurons.

The present data clearly show that neurons in LVb of both LEC and MEC give rise to dense intrinsic projections to more superficial layers and show laminar preferences (Fig. 6). We noticed a striking difference between the two entorhinal regions, in that neurons in LEC-LVb innervated LVa neurons, whereas in dorsal MEC this was rarely observed. In contrast, other intrinsic circuits from LVb to LII/III were very similar in both entorhinal subdivisions, which preferentially targeted pyramidal cells rather than the stellate or fan cells in LII. These data indicate that lack of experimental support for LVb to LVa projection in MEC is not due to technical issues and thus supports the conclusion that the dorsal parts of MEC lacks the canonical hippocampal-cortical output system.

Discussion

In this study, we experimentally tested the major assumption about the organization of hippocampal-cortical output circuits via entorhinal LVb neurons, considered to be crucial for the normal functioning of the medial temporal lobe memory system, more in particular systems memory consolidation. Our key finding is that LEC and MEC are strikingly different with respect to the hippocampal-cortical pathway mediated by LV neurons, in that we obtained electrophysiological evidence for the presence of this postulated crucial circuit in LEC, but not in MEC. In addition, we present new data that point to three major functionally relevant insights in the organization of the intrinsic translaminar entorhinal network originating from LVb neurons.

First, the present data indicate that LVb pyramidal neurons in LEC and MEC differ with respect to main morphological and electrophysiological characteristics. In contrast, LVa neurons in MEC and LEC are rather similar in these two aspects. Second, we show that projections from principal neurons in LVb in both entorhinal subdivisions preferentially synapse onto pyramidal neurons in LIII and LII. LVb neurons have a much weaker synaptic relationship with principal neurons in LII that project to the dentate gyrus (DG) and the CA3/CA2 region, i.e. stellate and fan cells. Last, and most important, our data point to a new and challenging circuit difference between the two entorhinal subdivisions with respect to the

inputs to LVa neurons, i.e. the output neurons of EC. Whereas in LEC, LVa neurons receive substantial input from LVb neurons, this projection is apparently weak to absent in MEC. The apparent lack of LVb-to-LVa projections in MEC, though unexpected in view of previous data including our own rabies tracing data (Ohara et al., 2018), has been recently corroborated in an *in vitro* study using paired-patch recording (Egorov et al., 2017), and is in line with a previous anterograde tracing study in the rat (Köhler, 1986).

Layer Vb neurons in LEC and MEC are morphologically and electrophysiologically different

With the use of specific transgenic mice in combination with expression-profiling of specific markers, we are the first to systematically differentiate between populations of entorhinal LV neurons. Our data allow us to differentiate neurons in LVa from those in LVb and to differentiate these layer specific neuron-types between LEC and MEC. This contrasts with previous studies in rats, showing that LV neurons in both LEC and MEC share electrophysiological properties (Canto and Witter, 2012a, 2012b; Hamam et al., 2000, 2002), although these authors did differentiate between LVa and LVb neurons based on morphological criteria and laminar distribution. We corroborate the reported morphological differences and add that the neurons also differ with respect to their electrophysiological properties. The most striking difference between MEC- and LEC-LVb neurons however is in the morphology of the apical dendrite. Neurons in MEC-LVb have an apical dendrite that heads straight to the pia, such that distal branches reach all the way up into LI, which is in line with previous studies (Canto and Witter, 2012a; Hamam et al., 2000; Sürmeli et al., 2015). In contrast, the apical dendrites of LEC-LVb neurons have a more complex branching pattern and they do not extend beyond LIII. This indicates that LEC-LVb neurons are unlikely to be targeted by inputs to LEC that selectively distribute to layers I and II, such as those carrying olfactory information from the olfactory bulb and the piriform cortex (Luskin and Price, 1983) as well as commissural projections (Leitner et al., 2016). The LVb neurons in LEC are thus dissimilar to their counterparts in MEC which are morphologically suited to receive such superficially terminating inputs, as has been shown for inputs from the parasubiculum (Canto et al., 2012) and contralateral MEC (Fuchs et al., 2016). The here reported differences between these LVb neurons, with MEC-LVb neurons showing a shorter time constant than LEC-LVb neurons, further indicates that MEC-LVb neurons have a shorter time window to integrate inputs compared to LEC-LVb neurons (Canto and Witter, 2012a, 2012b). Together, these differences likely contribute to differences in integration of information.

Layer Vb neurons preferentially target pyramidal neurons in layers III and II and avoid layer II neurons that project to the dentate gyrus.

Both our anatomical and electrophysiological data show that projections from principal neurons in LVb in both entorhinal subdivisions preferentially synapse onto pyramidal neurons in LIII and LII. LVb neurons have a much weaker synaptic relationship with the class of stellate and fan cells in MEC or LEC, respectively. This makes it likely that in both LEC and MEC, hippocampal information preferentially interacts with neurons that are part of the LIII-to-CA1/Sub projection system rather than with the LII-to-DG/CA2-3 projecting neurons. Additional target neurons in layer II/III might be the pyramidal neurons that project contralaterally, which in LII belong to the Calbindin (CB+) population (Ohara et al., 2019; Steward and Scoville, 1976; Varga et al., 2010), as well as the substantial population of CB+ excitatory intrinsic projection neurons (Ohara et al., 2019). The present findings are in line

with a previous study using wild type mice, reporting that most of the inputs to MEC-LII stellate cell arise from superficial layers, whereas those of MEC-LII pyramidal cells arise from the deep layers (Beed et al., 2010).

The sparse projection from MEC LVb neurons to LII stellate cells and the more massive projection to LII pyramidal cell, was unexpected for two reasons. First, both the stellate and the CB+ population of layer II pyramidal neurons contain grid cells (Hafting et al., 2005; Tang et al., 2014) and hippocampal excitatory inputs are required for the formation and translocation of grid patterns (Bonnevie et al., 2013). Though our data do not exclude that LVb inputs can reach LII stellate cells indirectly through LIII- and LII-pyramidal cells (Ohara et al., 2019; Winterer et al., 2017), they do indicate that the two populations of grid cells, stellate versus CB+ cells, might differ with respect to the strength of a main excitatory drive from the hippocampus.

Second, re-entry of hippocampal activity, i.e. the presence of recurrent circuits, have been proposed as one of the mechanisms for temporal storage of information in a neuronal network (Edelman, 1989; Iijima et al., 1996). Re-entry through LII-to-DG has been observed in *in vivo* recordings under anesthesia in rats, although this was examined with current source density analysis which is not optimal to exclude multisynaptic responses (Kloosterman et al., 2004). Such multisynaptic inputs could be mediated by pyramidal neurons in LIII and LII, both of which do contact layer II-to-DG projecting neurons (Ohara et al., 2019; Winterer et al., 2017). Our current data strongly favour the circuit via LIII-CA1/subiculum in both entorhinal subdivisions to mediate a recurrent hippocampal-entorhinal-hippocampal circuit. The importance of this layer III recurrent network is corroborated by the observation that entorhinal LIII input to the hippocampus field CA1 plays a crucial role in associating temporally discontinuous events and retrieving remote memories (Lux et al., 2016; Suh et al., 2011).

Layer Vb projections to layer Va exert prominent effects in LEC but not in MEC

Ever since the seminal observation in monkeys and rats of a hippocampal-cortical projection mediated by layer V of the entorhinal cortex (Kosel et al., 1982; Rosene and Van Hoesen, 1977), the canonical circuit underlying the hippocampal-cortical interplay, necessary for memory consolidation (Buzsáki, 1996; Eichenbaum et al., 2012), is believed to use EC LV neurons that receive hippocampal output and send projections to the neocortex. More recent studies in rats and mice indicated that neurons in LVb likely are the main recipients of this hippocampal output stream (Sürmeli et al., 2015) and that principal neurons in LVa form the main source of outputs to neocortical areas (Ohara et al., 2018; Sürmeli et al., 2015). The very sparse connection from LVb-to-LVa in MEC reported here thus indicates that at least in dorsal MEC, the canonical role of EC LV neurons to mediate hippocampal information transfer to downstream neocortical areas needs to be revised. In MEC, this output pathway apparently depends on a more complex multisynaptic local network. In contrast, our data in LEC show the presence of strong connections from LVb to LVa, and this striking difference is also reflected in the observation that LVa, the entorhinal-output layer, is thicker in LEC than in MEC. Together, this suggests that LEC might be the more relevant player in mediating the hippocampal-cortical interplay relevant for systems memory consolidation (Buzsáki, 1996; Eichenbaum et al., 2012; Frankland and Bontempi, 2005). However, studies which have functionally linked the LVa-output projection with memory consolidation are based on data obtained in MEC (Kitamura et al., 2017). This more likely reflects the strong focus on functions of MEC circuits rather than LEC circuits ever since the discovery of the grid cell (Hafting et al., 2005; Moser et al., 2017). With the discovery of LEC networks

coding for event sequences (Bellmund et al., 2019; Montchal et al., 2019; Tsao et al., 2018), this is likely to change.

Conclusion

Our experimental observations lead us to conclude that LEC might be more relevant than MEC in mediating the export of hippocampal information to the neocortex, a projection that allegedly is crucial to systems memory consolidation. In contrast, the two entorhinal subdivisions share the connectional motifs underlying transfer of hippocampal output back to the hippocampal formation, thus mediating re-entry. Finally, our data indicate that this re-entry circuit preferentially uses pyramidal neurons projecting to CA1 and subiculum and much less interacts with neurons projecting to the dentate gyrus and CA3/CA2.

Methods

Animals

All animals were group housed at a 12:12 h reversed day/night cycle and had ad libitum access to food and water. Mice of the transgenic MEC13-53D enhancer strain expressing tetracycline transactivator (tTA) in PCP4-positive entorhinal LVb neurons (Blankvoort et al., 2018) were used for whole-cell recordings (n=38), and for histological assessment of specific transgene expression (n=9). To characterize the tTA expression patterns in this mouse line, MEC13-53D was crossed with a tetO-GCaMP6-mCherry line (Blankvoort et al., 2018) (n=2). Other transgenic mouse lines, GAD67-GFP (Tanaka et al., 2003) (n=4) and Rosa26TdTomatoAi9 (Madisen et al., 2010) (n=2), were used to characterize entorhinal neurons in layer Va and Vb. All experiments were approved by the local ethics committee and were in accordance with the European Communities Council Directive and the Norwegian Experiments on Animals Act.

Viruses and Surgery

Animals were anesthetized with isoflurane in an induction chamber (4%, Nycomed, airflow 1 L/min), after which they were moved to a surgical mask on a stereotactic frame (Kopf Instruments). The animals were placed on a heating pad (37°C) to maintain stable body temperature throughout the surgery, and eye ointment was applied to the eyes of the animal to protect the corneas from drying out. The animals were injected subcutaneously with buprenorphine hydrochloride (0.1 mg/kg, Temgesic, Indivior), meloxicam (1 mg/kg, Metacam Boehringer Ingelheim Vetmedica), and bupivacaine hydrochloride (Marcain 1 mg/kg, Astra Zeneca), the latter at the incision site. The head was fixed to the stereotaxic frame with ear bars, and the skin overlying the skull at the incision site was disinfected with ethanol (70 %) and iodide before a rostrocaudal incision was made. A craniotomy was made around the approximate coordinate for the injection, and precise measurements were made with the glass capillary used for the virus injection. The coordinates of the injection sites are as follows (anterior to either bregma (APb) or transverse sinus (APt), lateral to sagittal sinus (ML), ventral to dura (DV) in mm): LEC (APt +2.0, ML 3.9, DV 3.0), MEC (APt +1.0, ML 3.3, DV 2.0), (NAc (APb +1.2, ML 1.0, DV 3.8), RSC (APb -3.0, ML 0.3, DV 0.8). Viruses were injected with a nanoliter injector (Nanoliter 2010, World Precision Instruments) controlled by a microsyringe pump controller (Micro4 pump, World Precision Instruments); 100–300 nl of virus was injected with a speed of 25 nl/min. The capillary was left in place for an additional 10 min after the injection, before it was slowly withdrawn from the brain. Finally, the wound was rinsed, and the skin was sutured. The animals were left to recover in a

heating chamber, before being returned to their home cage, where their health was checked daily.

For electrophysiological studies, young MEC13-53D mice (5 – 7 weeks old) were injected with a tTA-dependent adeno-associated virus (AAV, serotype 2/1) carrying either green fluorescent protein (GFP) or a fused protein of oChIEF, a variant of the light-activating protein channelrhodopsin2 (Lin et al., 2009), and citrine, a yellow fluorescent protein (Griesbeck et al., 2001). The construction of these virus, AAV-TRE-tight-GFP and AAV-TRE-tight-oChIEF-Citrine respectively, has been described in Nilssen et al (2018) . These samples were also used to characterize the transgenic mouse line and also the projection patterns of entorhinal LVb neurons. To label LVa neurons, retrograde AAV expressing enhanced blue fluorescent protein (EBFP) and Cre recombinase (AAVrg-pmSyn1-EBFP-cre, Addgene #51507) was injected into either NAc or RSC of Rosa26TdTomatoAi9. LVa neurons were also labelled in C57BL/6N mice, by injecting AAVrg-pmSyn1-EBFP-cre in NAc while injecting AAV-CMV-FLEX-mCherry in LEC/MEC. The pAAV-FLEX-mCherry-WPRE construct was created by first cloning a FLEX cassette with MCS into Cla1 and HindIII sites in pAAV-CMV-MCS-WPRE (Agilent) to create pAAV-CMV-FLEX-MCS-WPRE. The sequence of the FLEX cassette was obtained from Atasoy et al (2008). Subsequently, the mCherry sequence was synthesized and cloned in an inverted orientation into EcoR1 and BamH1 sites in pAAV-CMV-FLEX-MCS-WPRE to make pAAV CMV-FLEX-mCherry-WPRE. AAV-CMV-FLEX-mCherry was recovered from pAAV CMV-FLEX-mCherry-WPRE as described elsewhere (Nair et al., 2020; Nilssen et al., 2018).

Acute slice preparation

Two to three weeks after AAV injection, acute slice preparations were prepared as described in detail (Nilssen et al., 2018). Briefly, mice were deeply anesthetized with isoflurane and decapitated. The brain was quickly removed and immersed in cold (0°C) oxygenated (95% O_2/5% CO_2) artificial cerebrospinal fluid (ACSF) containing 110 mM choline chloride, 2.5 mM KCl, 25 mM D-glucose, 25 mM $NaHCO_3$, 11.5 mM sodium ascorbate, 3 mM sodium pyruvate, 1.25 mM NaH_2PO_4, 100 mM D-mannitol, 7 mM $MgCl_2$, and 0.5 mM $CaCl_2$, pH 7.4, 430 mOsm. The brain hemispheres were subsequently separated and 350 µm thick entorhinal slices were cut with a vibrating slicer (Leica VT1000S, Leica Biosystems). We used semicoronal slices for LEC recording, which were cut with an angle of 20° with respect to the coronal plane to optimally preserve neurons and local connections of LEC (Canto and Witter, 2012b; Nilssen et al., 2018). In case of MEC recordings, horizontal slices were prepared (Canto and Witter, 2012a; Couey et al., 2013). Slices were incubated in a holding chamber at 35°C in oxygenated ASCF containing 126 mM NaCl, 3 mM KCl, 1.2 mM Na_2HPO_4, 10 mM D-glucose, 26 mM $NaHCO_3$, 3 mM $MgCl_2$, and 0.5 mM $CaCl_2$ for 30 min and then kept at room temperature for at least 30 min before use.

Electrophysiological recording

Patch clamp recording pipettes (resistance:4-9 MΩ) were made from borosilicate glass capillaries (1.5 outer diameter x 0.86 inner diameter; Harvard Apparatus) and back-filled with internal solution of the following composition: 120 mM K-gluconate, 10 mM KCL, 10 mM Na_2-phosphocreatine, 10 mM HEPES, 4 mM Mg-ATP, 0.3 mM Na-GTP, with pH adjusted to 7.3 and osmolality to 300-305 mOsm. Biocytin (5 mg/mL; Iris Biotech) was added to the internal solution in order to recover cell morphology. Acute slices were moved to the recording setup and visualized using infrared differential interference contrast optics aided by a 20x/1.0 NA water immersion objective (Zeiss Axio Examiner D1, Carl Zeiss). Electrophysiological recordings were performed at 35°C and slices superfused with

oxygenated recording ACSF containing 126 mM NaCl, 3 mM KCl, 1.2 mM Na_2HPO_4, 10 mM D-Glucose, 26 mM $NaHCO_3$, 1.5 mM $MgCl_2$ and 1.6 mM $CaCl_2$. LVb in both LEC and MEC was identified through the presence of the densely packed small cells, and LVb neurons labelled with GFP were selected for recording. LVa neurons were selected for recording on the basis of their large soma size and the fact that they are sparsely distributed directly superficial to the small neurons of LVb. Gigaohm resistance seals were acquired for all cells before rupturing the membrane to enter whole-cell mode. Pipette capacitance compensation was performed prior to entering whole-cell configuration, and bridge balance adjustments were carried out at the start of current clamp recordings. Data acquisition was performed by Patchmaster (Heka Elektronik) controlling an EPC 10 Quadro USB amplifier (Heka Elektronik). Acquired data were low-pass Bessel filtered at 15.34 kHz (for whole-cell current-clamp recording) or 4 kHz (for whole-cell voltage-clamp recording) and digitized at 10 kHz. No correction was made for the liquid junction potential (13 mV as measured experimentally). Data were discarded if the resting membrane potential was ≥ -57 mV or/and the series resistance was ≥ 40 MΩ.

Intrinsic membrane properties were measured from membrane voltage responses to step injections of hyperpolarizing and depolarizing current (1 s duration, −200 pA to 200 pA, 20 pA increments). Acquired data were exported to text file with MATLAB (The MathWorks) and were analysed with Clampfit (Molecular Devices). The following electrophysiological parameters analysed were defined as follows:

Resting membrane potential (V_{rest}; mV): membrane potential measured with no current applied (I=0 mode);

Input resistance (Mohm): resistance measured from Ohm's law from the peak of voltage responses to hyperpolarizing current injections (-40 pA injection);

Sag ratio (steady-state/peak): measured from voltage responses to hyperpolarizing current injections with peaks at -90 ±5 mV, as the ratio between the voltage at steady-state and the voltage at the peak;

Action potential (AP) threshold (mV): the membrane potential where the rise of the action potential was 20 mV/ms;

AP peak (mV): voltage difference from AP threshold to peak;

AP half-width (ms): duration of the AP at half-amplitude from AP threshold;

AP maximum rate of rise (mV/ms): maximal voltage slope during the upstroke of the AP;

Fast afterhyperpolarization (fast AHP; in mV): the peak of AHP in a time window of 6 ms after the membrane potential reached 0mV during the repolarization phase of AP;

Medium AHP (mV): the peak of AHP in a time window of 200ms after fast AHP;

AP frequency after 200pA inj. (Hz): frequency of APs evoked with +200 pA of 1-s-long current injection;

Adaptation: measured from trains of 10±1 APs as [1 -(Ffirst/Flast)], where Ffirst and Flast are, respectively, the frequencies of the first and last interspike interval.

Optogenetic stimulation and patch-clamp data analysis

oChIEF+ fibers were photostimulated with a 473 nm laser controlled by a UGA-42 GEO point scanning system (Rapp OptoElectronic), and delivered through a 20×/1.0 NA WI

objective (Carl Zeiss Axio Examiner.D1). Laser pulses had a beam diameter of 36 µm and a duration of 1 ms. The tissue was illuminated with individual pulses at a rate of 1 Hz in a 4 × 5 grid pattern. Laser power was fixed to an intensity which evokes inward currents (EPSCs) but not action potentials. The voltage- or current-traces from individual stimulation spots were averaged over 4–6 individual sweeps to create an average response for each point in the 4 × 5 grid. The stimulation point which showed the largest voltage response was used for further analysis. Deflections of the average voltage trace exceeding 10 SDs (±10 SDs) of the baseline were classified as synaptic responses. Postsynaptic potentials were calculated as the difference between the peak of the evoked synaptic potential and the baseline potential measured before stimulus onset. The latency of optical activation was defined as the time interval between light onset and the point where the voltage trace exceeded 10% amplitude. Data analysis was performed using custom-written scripts in MATLAB. Disynaptic inhibitory inputs were detected in voltage-clamp mode by holding the membrane potential at either -55 mV or 0 mV and examining the presence of outward current.

All data presented in the figures are shown as mean ± standard errors. Prism software was used for data analysis (Graphpad software), and one-way ANOVA with Bonferroni's multiple comparison test was used to compare the electrophysiological properties and voltage responses between each cell types. To analyze mediolateral gradient in LVb-to-LVa connectivity of MEC, we used Pearson correlation coefficient. A principal component analysis based on the 12 electrophysiological properties (Supplementary Table 1) was conducted in MATLAB. For this purpose, all variables were normalized to a standard deviation of 1.

Histology, Immunohistochemistry, and imaging of electrophysiological slices

After electrophysiological recordings, the brain slices were put in 4% paraformaldehyde (PFA, Merck Chemicals) in 0.1 M phosphate buffer (PB) for 48 h at 4°C. Slices were permeabilized 5 × 15 min in phosphate buffered saline containing 0.3% Triton X-100 (PBS-Tx), and were immersed in a blocking solution containing PBS-TX and 10% Normal Goat Serum (NGS, Abcam: AB7481) for three hours at room temperature. To visualized targeted entorhinal LVb neurons, slices were incubated with a primary antibody, chicken anti-GFP (1:500, Abcam), diluted in the blocking solution for 4 days at 4°C. After this, the sections were washed 5 × 15 min in PBS-Tx at room temperature and incubated in a secondary antibody, goat anti-chicken (1:400, Alexa Fluor 488, Thermo Fisher Scientific) overnight at room temperature. This secondary antibody incubation was accompanied with the fluorescent conjugated streptavidin (1:600, AF546, Thermo Fisher Scientific) and Neurotrace 640/660 deep-red fluorescent nissl stain (1:200, Thermo Fisher Scientific) in order to stain cells filled with biocytin and to identify the cytoarchitecture. Slices were rinsed in PBS-TX (3 × 10 min) at and dehydrated by increasing ethanol concentrations (30%, 50%, 70%, 90%, 100%, 100%, 10 min each). They were treated to a 1:1 mixture of 100% ethanol and methyl salicylate for 10 minutes before clearing and storage in methyl salicylate (VWR Chemicals).

To image the recorded neurons with a laser scanning confocal microscope (Zeiss LSM 880 AxioImager Z2), the slices were mounted in custom-made metal well slides with methyl salicylate and coverslipped. Overview images of the tissue were taken at low magnification (Plan-Apochromat 10×, NA 0.45) to confirm the location of the recorded neurons, and at higher magnification (Plan-Apochromat 20×, NA 0.8) to determine the morphology of the recorded neurons. Both overview images and high-magnification images were obtained as z stacks that included the whole extent of each recorded cell to recover the full cell morphology. The morphology of LVb neurons of MEC/LEC was classified based on previous studies (Canto and Witter, 2012a, 2012b; Hamam et al., 2000, 2002).

Histology, immunohistochemistry, and imaging of neuroanatomical tracing samples

After two to three weeks of survival, virus-injected mice were anesthetized with isoflurane before being euthanized with a lethal intraperitoneal injection of pentobarbital (100 mg/kg, Apotekerforeningen). They were subsequently transcardially perfused using a peristaltic pump (World Precision Instruments), first with Ringer's solution (0.85% NaCl, 0.025% KCl, 0.02% NaHCO3) and subsequently with freshly prepared 4% PFA in 0.1 M PB (pH 7.4). The brains were removed from the skull, postfixed in PFA overnight, and put in a cryo-protective solution containing 20% glycerol, 2% DMSO diluted in 0.125 m PB. A freezing microtome was used to cut the brains into 40-µm-thick sections, that were collected in six equally spaced series for processing.

To enhance the GFP signal in AAV-TRE-tight-GFP/oChIEF-Citrine infected entorhinal LVb neurons and in GAD67-positive neurons, sections were stained with primary (1:400, chicken anti-GFP, Abcam #ab13970; 1:2000, rabbit anti-GFP, Thermo Fisher Scientific #A11122) and secondary antibodies (1:400, AlexaFluor-488 goat anti-chicken IgG, Thermo Fisher Scientific #A11039; 1:400, Alexa Fluor-546 goat anti-rabbit IgG, Thermo Fisher Scientific #A11010). To identify the LVb border and to characterize the transgenic mouse line, LVb neurons were visualized with primary (1:300, rabbit anti-PCP4, Sigma Aldrich #HPA005792; 1:3000, rat anti-Ctip, Abcam #ab18465) and secondary antibodies (1:400, Alexa Fluor 633 goat anti-rat IgG, Thermo Fisher Scientific # A21094; 1:400, Alexa Fluor-546 goat anti-rabbit IgG; 1:400, Alexa Fluor 635 goat anti-rabbit IgG, Thermo Fisher Scientific # A31576). For delineation purpose, sections were stained with primary (1:1000, guinea pig anti-NeuN, Millipore #ABN90P; 1:1000, mouse anti-NeuN, Millipore #MAB377) and secondary antibodies (1:400, Alexa Fluor 647 goat anti-guinea pig IgG, Thermo Fisher Scientific #A21450; 1:400, Alexa Fluor 488 goat anti-guinea pig IgG, Thermo Fisher Scientific #A11073; 1:400, Alexa Fluor 488 goat anti-mouse IgG, Thermo Fisher Scientific #A11001).

For all immunohistochemical staining except for Ctip2-staining, we used the same procedure. Sections were rinsed 3 × 10 min in PBS-Tx followed by 60 min incubation in a blocking solution containing PBS-Tx with either 5% NGS or 3% Bovine serum albumin (BSA). Sections were incubated with the primary antibodies diluted in the blocking solution for 48 h at 4°C, rinsed 3 × 10 min in PBS-Tx, and incubated with secondary antibodies diluted in PBS-Tx overnight at room temperature. Finally, sections were rinsed 3 × 10 min in PBS. For Ctip2-staining, sections were heated to 80˚C for 15 minutes in 10 mM sodium citrate (SC, pH 8.5). After cooling to room temperature, the sections were permeabilized by washing them 3 times in SC buffer containing 0.3 % Triton X-100 (SC-Tx) and subsequently pre-incubated in a blocking solution containing SC-Tx and 3 % BSA for one hour at room temperature. Next, sections were incubated with the primary antibodies diluted in the blocking solution for 48 h at 4°C, rinsed 2 × 15 min in SC-Tx and 1%BSA, and incubated with secondary antibodies diluted in SC-Tx and 1%BSA for overnight at room temperature. Finally, sections were rinsed 3 × 10 min in PBS. After staining, sections were mounted on SuperfrostPlus microscope slides (Thermo Fisher Scientific) in Tris-gelatin solution (0.2% gelatin in Tris-buffer, pH 7.6), dried, and coverslipped with entellan in a toluene solution (Merck Chemicals, Darmstadt, Germany).

Coverslipped samples were imaged using an Axio ScanZ.1 fluorescent scanner, equipped with a 10× objective, Colibri.2 LED light source, and a quadruple emission filter (Plan-Apochromat 10×, NA 0.45, excitation 488/546, emission 405/488/546/633, Carl Zeiss). To quantify the colocalization of GFP-, PCP4-, and Ctip2-immunolabeling, confocal images were acquired in sections taken at every 240 µm throughout the entorhinal cortex, using a

confocal microscope (Zeiss LSM 880 AxioImager Z2) with a 40× oil objective (Plan Apochromat 40× oil, NA 1.3, Carl Zeiss). The number of immunohistochemically labelled neurons was quantified in a fixed Z-level of the confocal images using Image J software (http://rsb.info.nih.gov/ij).

Delineations of EC layers

The border of superficial layers (I-III) and the thin acellular layer IV (lamina dissecans) were delineated based on previous studies (Insausti et al., 1997). Layers Va and Vb were differentiated based on cell size, cell density, cell marker, and the projection patterns. LVb neurons are densely packed small cells that are PCP4-positive, whereas LVa is made up of sparsely distributed large cells which project to various cortical- and subcortical regions (Supplementary Fig. 1) (Kitamura et al., 2017; Ohara et al., 2018; Sürmeli et al., 2015). The border between layer Vb and VI is more difficult to identify, since PCP4-staining also labels LVI neurons. We determined this border based on the cell density which decreases in LVI. In case of MEC, the border can also be identified since the typical columnar organization of LVb stops upon entering LVI.

Statistics

Statistical analyses were performed using GraphPad Prism (GraphPad Software) or MATLAB (MathWorks). The details of tests used are described with the results. Differences between the groups were tested using paired and unpaired t-tests. Group comparisons were made using one-way ANOVA followed by Bonferroni post-hoc tests to control for multiple comparisons. All statistical tests were two-tailed, and thresholds for significance were placed at $*p < 0.05$, $**p < 0.01$, and $***p < 0.001$. All data are shown as mean ± SEM. No statistical methods were used to pre-determine sample size but the number of mice and cells for each experiment is similar with previous studies in the field (Doan et al., 2019; Nilssen et al., 2018). Mice were randomly selected from both sexes, and all experiments were successfully replicated in several samples. No blinding was used during data acquisition, but electrophysiological data analyses were performed blind to groups.

Conflict of interest statement.

The authors do not report a conflict of interest.

Author contributions

SO, MPW, MJN, and ESN conceived the study design. The experimental data was collected by SO and analysed by SO with help of MJN and ESN. SB produced the transgenic mouse line and RRN produced the AAV vectors, both under supervision of CGK. All authors contributed to the discussions that resulted in the current paper, which was written by SO and MPW, and edited by CGK. All authors approved the final version of the manuscript.

Funding

This work has been supported by the Kavli Foundation, the Centre of Excellence scheme – Centre for Neural Computation and research grant # 227769 of the Research Council of Norway, The Egil and Pauline Braathen and Fred Kavli Centre for Cortical Microcircuits,

and the National Infrastructure scheme of the Research Council of Norway – NORBRAIN #197467. This work has also been supported by Grant-in-Aid for Scientific Research (KAKENHI, #19K06917) from the Ministry of Education, Culture, Sports, Science and Technology (MEXT) of Japan.

Acknowledgments

We thank Grethe M. Olsen and Paulo Girao for help with histological preparations and microscopical imaging, and Paulo Girao and Yasutaka Honda for MATLAB programming.

References

Alonso, a, Klink, R., 1993. Differential electroresponsiveness of stellate and pyramidal-like cells of medial entorhinal cortex layer II. J. Neurophysiol. 70(1), 128–143.

Atasoy, D., Aponte, Y., Su, H.H., Sternson, S.M., 2008. A FLEX switch targets channelrhodopsin-2 to multiple cell types for imaging and long-range circuit mapping. J. Neurosci. 28(28), 7025–7030.

Beed, P., Bendels, M.H.K., Wiegand, H.F., Leibold, C., Johenning, F.W., Schmitz, D., 2010. Analysis of Excitatory Microcircuitry in the Medial Entorhinal Cortex Reveals Cell-Type-Specific Differences. Neuron 68(6), 1059–1066.

Bellmund, J.L., Deuker, L., Doeller, C.F., 2019. Mapping sequence structure in the human lateral entorhinal cortex. Elife 8.

Blankvoort, S., Witter, M.P., Noonan, J., Cotney, J., Kentros, C., 2018. Marked Diversity of Unique Cortical Enhancers Enables Neuron-Specific Tools by Enhancer-Driven Gene Expression. Curr. Biol. 28(13), 2103-2114.e5.

Bonnevie, T., Dunn, B., Fyhn, M., Hafting, T., Derdikman, D., Kubie, J.L., Roudi, Y., Moser, E.I., Moser, M.B., 2013. Grid cells require excitatory drive from the hippocampus. Nat. Neurosci. 16(3), 309–317.

Buzsáki, G., 1996. The hippocampo-neocortical dialogue. Cereb. Cortex 6, 81–92.

Canto, C.B., Koganezawa, N., Beed, P., Moser, E.I., Witter, M.P., 2012. All Layers of Medial Entorhinal Cortex Receive Presubicular and Parasubicular Inputs. J. Neurosci. 32(49), 17620–17631.

Canto, C.B., Witter, M.P., 2012a. Cellular properties of principal neurons in the rat entorhinal cortex. II. The medial entorhinal cortex. Hippocampus 22(6), 1277–1299.

Canto, C.B., Witter, M.P., 2012b. Cellular properties of principal neurons in the rat entorhinal cortex. I. The lateral entorhinal cortex. Hippocampus 22(6), 1256–1276.

Couey, J.J., Witoelar, A., Zhang, S.J., Zheng, K., Ye, J., Dunn, B., Czajkowski, R., Moser, M.B., Moser, E.I., Roudi, Y., Witter, M.P., 2013. Recurrent inhibitory circuitry as a mechanism for grid formation. Nat. Neurosci. 16(3), 318–24.

Deshmukh, S.S., Knierim, J.J., 2011. Representation of Non-Spatial and Spatial Information in the Lateral Entorhinal Cortex. Front. Behav. Neurosci. 5(69).

Doan, T.P., Lagartos-Donate, M.J., Nilssen, E.S., Ohara, S., Witter, M.P., 2019. Convergent Projections from Perirhinal and Postrhinal Cortices Suggest a Multisensory Nature of Lateral, but Not Medial, Entorhinal Cortex. Cell Rep. 29(3), 617-627.e7.

Edelman, G.M., 1989. The Remembered Present : A Biological Theory of Consciousness. Basic Books.

Egorov, A. V., Lorenz, F.S., Rozov, A., Draguhn, A., 2017. Local circuitry in the medial entorhinal cortex layer V. SfN Abstr. 474.09.

Eichenbaum, H., Sauvage, M., Fortin, N., Komorowski, R., Lipton, P., 2012. Towards a functional organization of episodic memory in the medial temporal lobe. Neurosci. Biobehav. Rev. 36(7), 1597–1608.

Frankland, P.W., Bontempi, B., 2005. The organization of recent and remote memories. Nat. Rev. Neurosci. 6(2), 119–130.

Fuchs, E.C., Neitz, A., Pinna, R., Melzer, S., Caputi, A., Monyer, H., 2016. Local and Distant Input Controlling Excitation in Layer II of the Medial Entorhinal Cortex. Neuron 89(1), 194–208.

Griesbeck, O., Baird, G.S., Campbell, R.E., Zacharias, D.A., Tsien, R.Y., 2001. Reducing the environmental sensitivity of yellow fluorescent protein. Mechanism and applications. J. Biol. Chem. 276(31), 29188–94.

Hafting, T., Fyhn, M., Molden, S., Moser, M.B., Moser, E.I., 2005. Microstructure of a spatial map in the entorhinal cortex. Nature 436(7052), 801–806.

Hamam, B.N., Amaral, D.G., Alonso, A.A., 2002. Morphological and electrophysiological characteristics of layer V neurons of the rat lateral entorhinal cortex. J. Comp. Neurol. 451(1), 45–61.

Hamam, B.N., Kennedy, T.E., Alonso, A., Amaral, D.G., 2000. Morphological and electrophysiological characteristics of layer V neurons of the rat medial entorhinal cortex. J. Comp. Neurol. 418(4), 457–472.

Iijima, T., Witter, M.P., Ichikawa, M., Tominaga, T., Kajiwara, R., Matsumoto, G., 1996. Entorhinal-hippocampal interactions revealed by real-time imaging. Science 272(5265), 1176–1179.

Insausti, R., Herrero, M.T., Witter, M.P., 1997. Entorhinal cortex of the rat: cytoarchitectonic subdivisions and the origin and distribution of cortical efferents. Hippocampus 7(2), 146–83.

Kitamura, T., Ogawa, S.K., Roy, D.S., Okuyama, T., Morrissey, M.D., Smith, L.M., Redondo, R.L., Tonegawa, S., 2017. Engrams and circuits crucial for systems consolidation of a memory. Science 356(6333), 73–78.

Kloosterman, F., van Haeften, T., Lopes da Silva, F.H., 2004. Two reentrant pathways in the hippocampal-entorhinal system. Hippocampus 14(8), 1026–1039.

Köhler, C., 1986. Intrinsic connections of the retrohippocampal region in the rat brain. II. The medial entorhinal area. J. Comp. Neurol. 246(2), 149–169.

Köhler, C., 1985. Intrinsic projections of the retrohippocampal region in the rat brain. I. The subicular complex. J. Comp. Neurol. 236(4), 504–22.

Kosel, K.C., Van Hoesen, G.W., Rosene, D.L., 1982. Non-hippocampal cortical projections from the entorhinal cortex in the rat and rhesus monkey. Brain Res. 244(2), 201–213.

Leitner, F.C., Melzer, S., Lütcke, H., Pinna, R., Seeburg, P.H., Helmchen, F., Monyer, H., 2016. Spatially segregated feedforward and feedback neurons support differential odor processing in the lateral entorhinal cortex. Nat. Neurosci. 19(7), 935–944.

Lin, J.Y., Lin, M.Z., Steinbach, P., Tsien, R.Y., 2009. Characterization of engineered channelrhodopsin variants with improved properties and kinetics. Biophys. J. 96(5), 1803–14.

Luskin, M.B., Price, J.L., 1983. The topographic organization of associational fibers of the olfactory system in the rat, including centrifugal fibers to the olfactory bulb. J. Comp. Neurol. 216, 264–291.

Lux, V., Atucha, E., Kitsukawa, T., Sauvage, M.M., 2016. Imaging a memory trace over half a life-time in the medial temporal lobe reveals a time-limited role of CA3 neurons in retrieval. Elife 5.

Madisen, L., Zwingman, T.A., Sunkin, S.M., Oh, S.W., Zariwala, H.A., Gu, H., Ng, L.L., Palmiter, R.D., Hawrylycz, M.J., Jones, A.R., Lein, E.S., Zeng, H., 2010. A robust and high-throughput Cre reporting and characterization system for the whole mouse brain. Nat. Neurosci. 13(1), 133–140.

Montchal, M.E., Reagh, Z.M., Yassa, M.A., 2019. Precise temporal memories are supported by the lateral entorhinal cortex in humans. Nat. Neurosci. 22(2), 284–288.

Moser, E.I., Moser, M.B., McNaughton, B.L., 2017. Spatial representation in the hippocampal formation: A history. Nat. Neurosci. 20(11), 1448–1464.

Nadel, L., Moscovitch, M., 1997. Memory consolidation, retrograde amnesia and the hippocampal complex. Curr. Opin. Neurobiol. 7(2), 217–227.

Nair, R.R., Blankvoort, S., Lagartos, M.J., Kentros, C., 2020. Enhancer-Driven Gene Expression (EDGE) Enables the Generation of Viral Vectors Specific to Neuronal Subtypes. iScience 23(3), 100888.

Nilssen, E.S., Jacobsen, B., Fjeld, G., Nair, R.R., Blankvoort, S., Kentros, C., Witter, M.P., 2018. Inhibitory connectivity dominates the fan cell network in layer II of lateral entorhinal cortex. J. Neurosci. 38(45), 9712–9727.

Ohara, S., Gianatti, M., Itou, K., Berndtsson, C.H., Doan, T.P., Kitanishi, T., Mizuseki, K., Iijima, T., Tsutsui, K.I., Witter, M.P., 2019. Entorhinal Layer II Calbindin-Expressing Neurons Originate Widespread Telencephalic and Intrinsic Projections. Front. Syst. Neurosci. 13(54).

Ohara, S., Onodera, M., Simonsen, Ø.W., Yoshino, R., Hioki, H., Iijima, T., Tsutsui, K.I., Witter, M.P., 2018. Intrinsic Projections of Layer Vb Neurons to Layers Va, III, and II in the Lateral and Medial Entorhinal Cortex of the Rat. Cell Rep. 24(1), 107–116.

Rosene, D.L., Van Hoesen, G.W., 1977. Hippocampal efferents reach widespread areas of cerebral cortex and amygdala in the rhesus monkey. Science 198(4314), 315–317.

Squire, L.R., Alvarez, P., 1995. Retrograde amnesia and memory consolidation: a neurobiological perspective. Curr. Opin. Neurobiol. 5(2), 169–177.

Steffenach, H.A., Witter, M.P., Moser, M.B., Moser, E.I., 2005. Spatial memory in the rat requires the dorsolateral band of the entorhinal cortex. Neuron 45(2), 301–313.

Stensola, H., Stensola, T., Solstad, T., Froland, K., Moser, M.-B., Moser, E.I., 2012. The entorhinal grid map is discretized. Nature 492(7427), 72–78.

Steward, O., Scoville, S.A., 1976. Cells of origin of entorhinal cortical afferents to the hippocampus and fascia dentata of the rat. J. Comp. Neurol. 169(3), 347–70.

Suh, J., Rivest, A.J., Nakashiba, T., Tominaga, T., Tonegawa, S., 2011. Entorhinal cortex layer III input to the hippocampus is crucial for temporal association memory. Science 334(6061), 1415–1420.

Sürmeli, G., Marcu, D.C., McClure, C., Garden, D.L.F., Pastoll, H., Nolan, M.F., 2015. Molecularly Defined Circuitry Reveals Input-Output Segregation in Deep Layers of the Medial Entorhinal Cortex. Neuron 88(5), 1040–1053.

Tanaka, D., Nakaya, Y., Yanagawa, Y., Obata, K., Murakami, F., 2003. Multimodal tangential migration of neocortical GABAergic neurons independent of GPI-anchored proteins. Development 130(23), 5803–13.

Tang, Q., Burgalossi, A., Ebbesen, C.L., Ray, S., Naumann, R., Schmidt, H., Spicher, D., Brecht, M., 2014. Pyramidal and stellate cell specificity of grid and border representations in layer 2 of medial entorhinal cortex. Neuron 84(6), 1191–1197.

Tsao, A., Moser, M.B., Moser, E.I., 2013. Traces of experience in the lateral entorhinal cortex. Curr. Biol. 23(5), 399–405.

Tsao, A., Sugar, J., Lu, L., Wang, C., Knierim, J.J., Moser, M.-B., Moser, E.I., 2018. Integrating time from experience in the lateral entorhinal cortex. Nature 561(7721), 57–62.

van Haeften, T., Baks-te-Bulte, L., Goede, P.H., Wouterlood, F.G., Witter, M.P., 2003. Morphological and numerical analysis of synaptic interactions between neurons in deep and superficial layers of the entorhinal cortex of the rat. Hippocampus 13(8), 943–952.

Varga, C., Lee, S.Y., Soltesz, I., 2010. Target-selective GABAergic control of entorhinal cortex output. Nat. Neurosci. 13(7), 822–4.

Winterer, J., Maier, N., Wozny, C., Beed, P., Breustedt, J., Evangelista, R., Peng, Y., Albis, T.D., Kempter, R., Schmitz, D., 2017. Excitatory microcircuits within superficial layers of the medial entorhinal cortex. Cell Rep. 1247, 1110–1116.

Xu, W., Wilson, D.A., 2012. Odor-evoked activity in the mouse lateral entorhinal cortex. Neuroscience 223, 12–20.

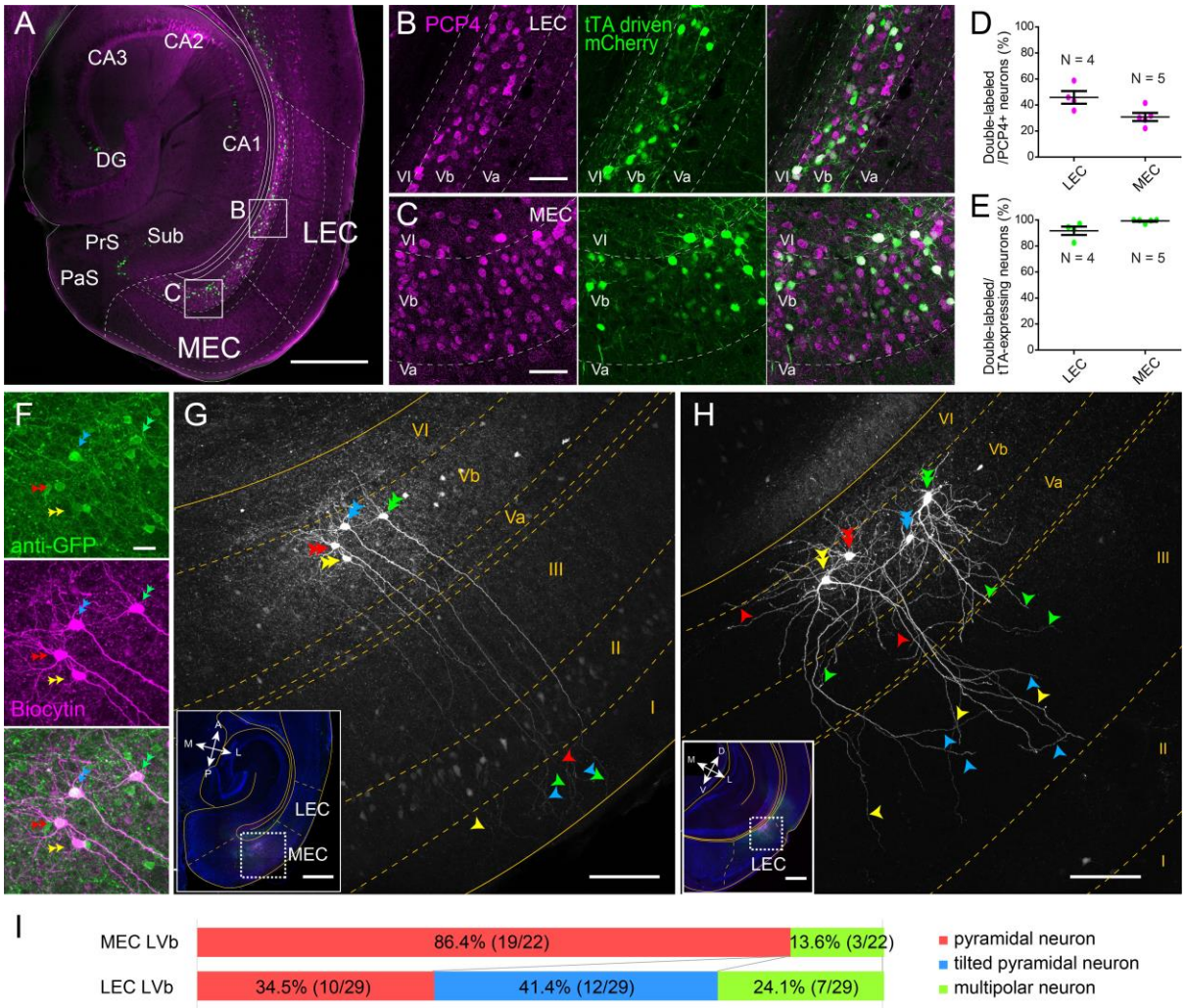

Figure 1. LEC and MEC LVb neurons show distinct morphological features.

A-C, Expression of tTA in the EDGE mouse line (MEC-13-53D), which is visualized with mCherry (green) by crossing to tTA-dependent mCherry line. A horizontal section was immunostained with an anti-PCP4 antibody (magenta) to label entorhinal LVb neurons. Images of LEC (B) and MEC (C) correspond with the boxed areas in (A). **D**, Percentage of tTA-expressing neurons among the total PCP4-positive neurons in LEC and MEC. **E**, Percentage of PCP4-positive neurons among the total tTA-expressing neurons in LEC and MEC. Error bars: mean ± SEM. The tTA-expressing neurons mainly distributed in LVb of EC and colocalized with PCP4. **F-H**, Morphology of LVb neurons targeted in MEC-13-53D in MEC (F-G) and LEC (H). tTA-expressing LVb neurons were first labelled with GFP (green) by injecting AAV2/1-TRE-Tight-EGFP in MEC-13-53D, and then intracellularly filled with biocytin (magenta, F). Images of MEC (G) and LEC (H) show biocytin labeling which correspond with the boxed area in each inset. The four neurons shown in (F) correspond to the neurons in (G). Double arrowheads show the cell body while the single arrowheads show their dendrites, and different neurons are marked in different colors (green, blue, red, and yellow). The distribution of apical dendrites largely differs between MEC-LVb and LEC-LVb neurons. **I**, Proportion of morphologically identified cell types of LVb neurons in LEC and MEC. These data were obtained in 10 animals and 22 slices. Scale bars represent 500 μm for (A) and inset of (G) and (H), 100 μm for (G) and (H), 50 μm for (B) and (C), and 20 μm for (F).

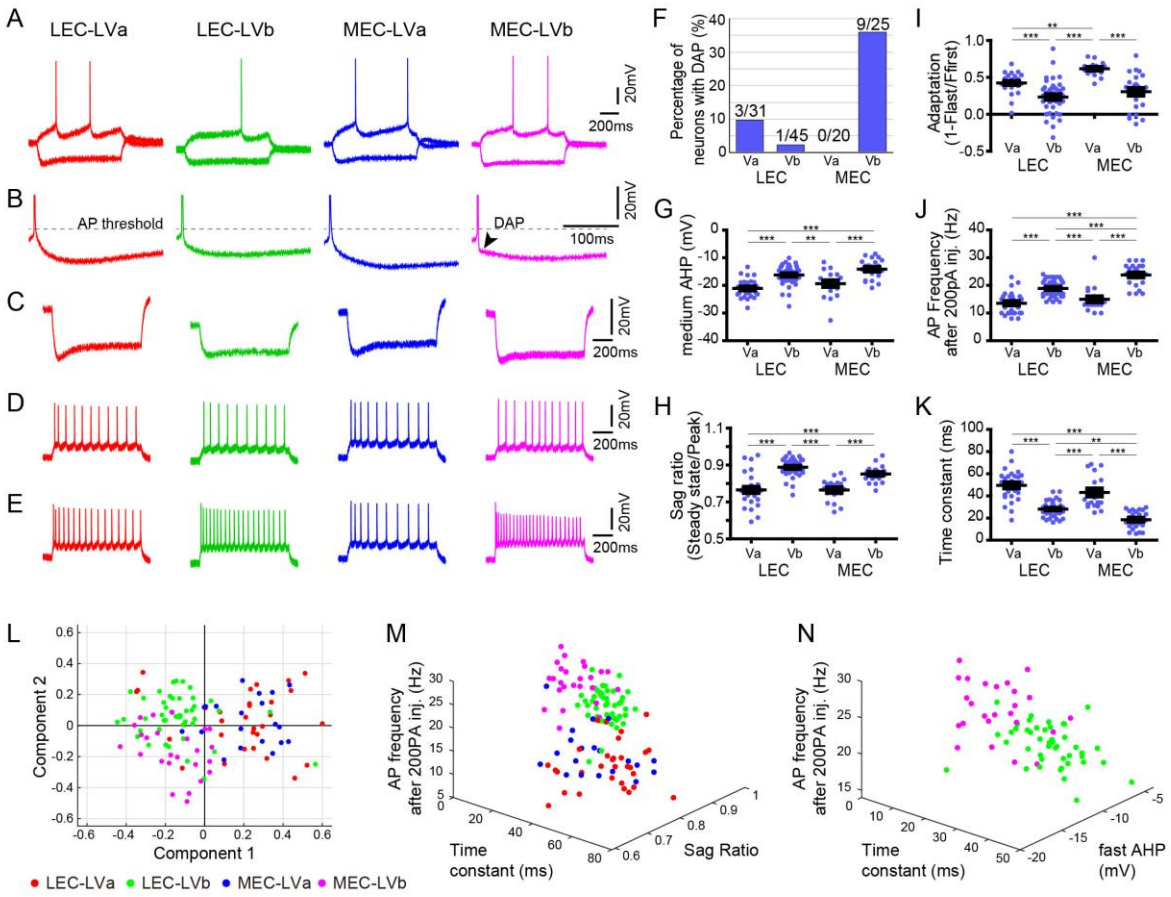

Figure 2. Electrophysiological properties distinguish LVa/LVb neurons in both LEC and MEC.

A, Representative voltage responses to hyperpolarizing and depolarizing current injection of LEC-LVa (red), LEC-LVb (green), MEC-LVa (blue), and MEC-LVb (magenta) neurons. **B**, Voltage responses at rheobase current injections showing AHP wave form and DAP. **C**, Voltage responses to hyperpolarizing current injection with peaks at -90 ± 5 mV showing Sag. **D**, Voltage responses to depolarizing current injection with 10 ± 1 APs showing adaptation. **E**, Voltage responses to +200 pA of 1-s-long current injection showing maximal AP number. **F**, Percentage of LV neurons with DAP. **G-K**, Differences of medium AHP (G, one-way ANOVA, $F_{3,117} = 21.99$, ***$p < 0.0001$, Bonferroni's multiple comparison test, **$p < 0.01$, ***$p < 0.001$), sag ratio (H, one-way ANOVA, $F_{3,117} = 36.88$, ***$p < 0.0001$, Bonferroni's multiple comparison test, ***$p < 0.001$), adaptation (I, one-way ANOVA, $F_{3,117} = 21.6$, ***$p < 0.0001$, Bonferroni's multiple comparison test, **$p < 0.01$, ***$p < 0.001$), AP frequency after 200 pA injection (J, one-way ANOVA, $F_{3,117} = 44.37$, ***$p < 0.0001$, Bonferroni's multiple comparison test, ***$p < 0.001$), and time constant (K, one-way ANOVA, $F_{3,117} = 53.39$, ***$p < 0.0001$, Bonferroni's multiple comparison test, **$p < 0.01$, ***$p < 0.001$) between LEC-LVa (N=31), LEC-LVb (N=45), MEC-LVa (N=20), and MEC-LVb (N=25) neurons (Error bars: mean ± standard errors). **L**, Principal component analysis based on the twelve electrophysiological parameters shown in Supplementary Table 1 show a separation between LVa and LVb neurons as well as a moderate separation between LEC-LVb and MEC-LVb neurons. Data representing 121 neurons from 27 animals (also holds for M and N). **M**, Separation of LEC-LVa (red), LEC-LVb (green), MEC-LVa (blue), and MEC-LVb (magenta) neurons using sag ratio, AP frequency at 200 pA injection, and time constant as

distinction criteria. **N**, Separation of LEC-LVb (green) and MEC-LVb (magenta) neurons using fast AHP, AP frequency at 200 pA injection, and time constant as distinction criteria.

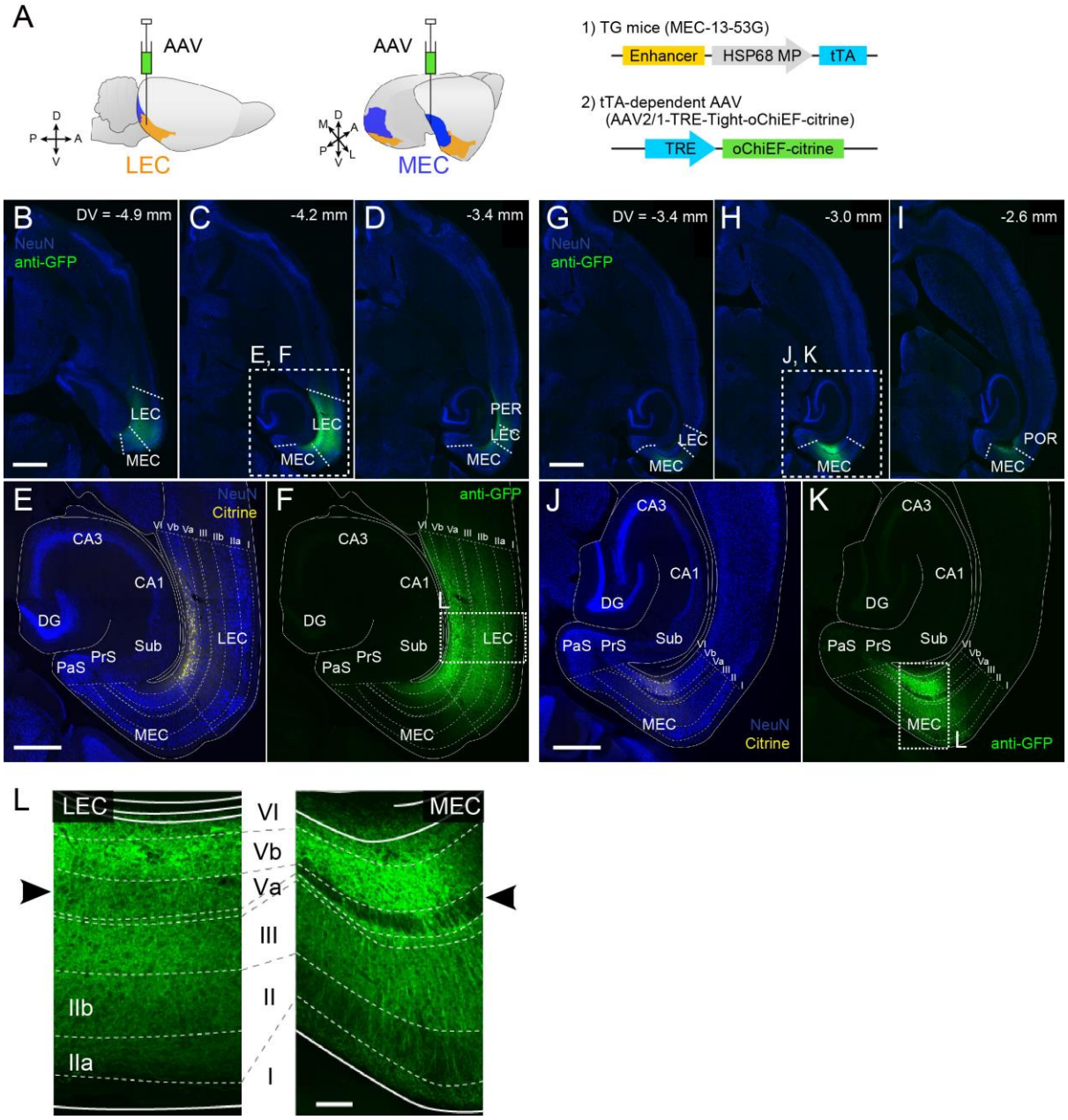

Figure 3. LVb neurons project locally, and their projections differ between LEC- and MEC.

A. tTA-expressing entorhinal LVb neurons were visualized by injecting a tTA-dependent AAV expressing oChiEF-citrine into either LEC or MEC of MEC-13-53G. **B-F**, Horizontal sections showing distribution of labelled neurites originating from LEC-LVb at different dorsoventral levels (B-D). Images of EC (E, F) corresponds to the boxed area in (C). Note that the cell bodies of labelled neurons are located in LVb of LEC (citrine labels in yellow, E), and that the labelled neurites mainly distribute within EC (anti-GFP labels in green, F). The labelling observed in perirhinal cortex (PER; D) originate from the sparse infection of PER neurons due to the leakage of the virus along the injection tract. **G-K**, Horizontal sections showing distribution of labelled fibers originating from MEC-LVb at different dorsoventral level (G-I). Images of EC (J, K) corresponds to the boxed area in (H). Note that the cell bodies of labelled neurons are located in LVb of MEC (J), and that the labelled neurites mainly distribute within EC (K). The labelling observed in postrhinal cortex (POR; I) originate from the sparse infection of POR neurons due to the leakage of the virus along the

injection tract. **L**, Comparison of GFP expression patterns originating from LEC-LVb and MEC-LVb neurons. The left panel corresponds to the boxed area in (F) and is 90 degrees rotated to match the orientation of the right panel, which represent the boxed area in (K). The distribution of the labelled fibers is strikingly different between LEC and MEC in LVa (black arrowhead) with strong terminal projection in LEC and almost absent projection in LVa of MEC. Scale bars represent 1,000 μm for (B) and (G) (also apply to C, D, H, I), 500 μm for (E) and (J) (also apply to F and K), 100 μm for (L).

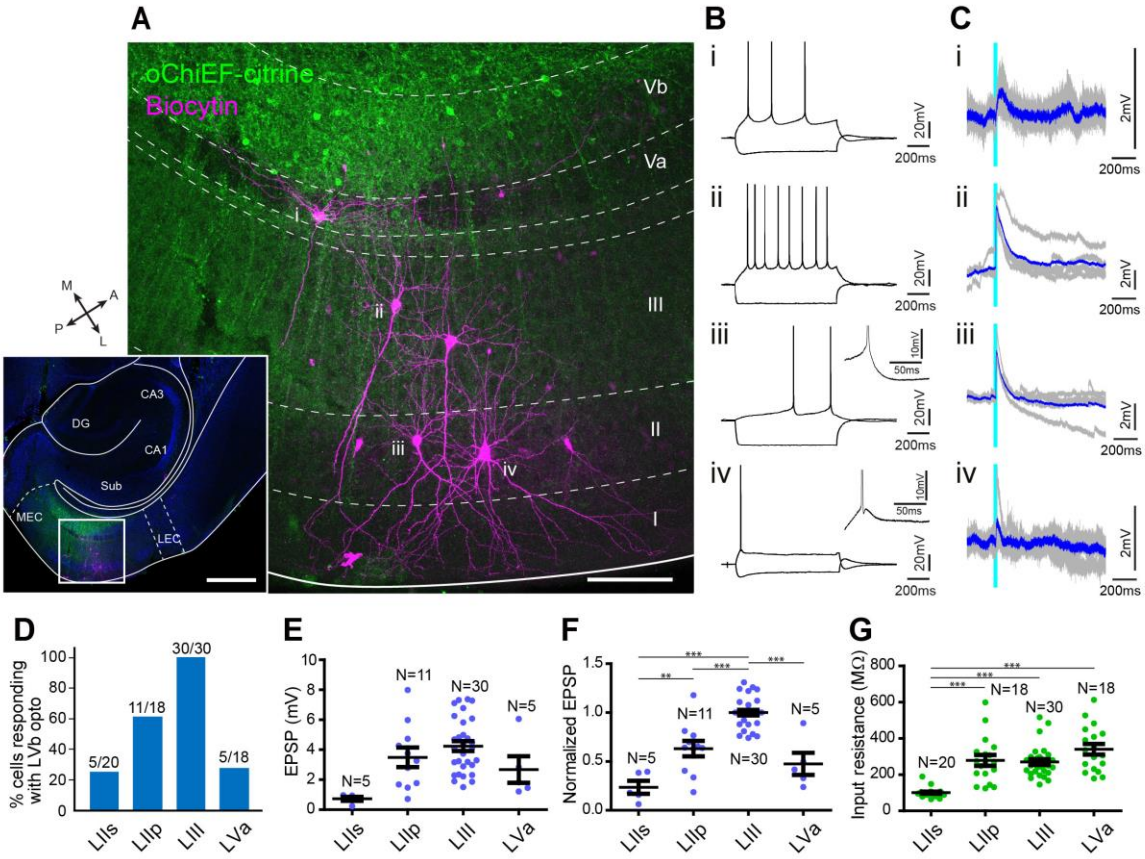

Figure 4. MEC-LVb neurons preferentially target LII/III pyramidal neurons.

A, Image of a representative horizontal slice showing expression of oChiEF-citrine in LVb neurons (green), and recorded neurons labelled with biocytin (magenta) in MEC. Inset shows a low power image of the section indicating the position of the higher power image. Scale bars represent 500 µm (inset) and 100 µm. **B**, Voltage responses to injected current steps recorded from neurons shown in (A): i, pyramidal cell in LVa; ii, pyramidal cell in LIII; iii, pyramidal cell in LII; iv, stellate cell in LII. Inset in (iii) and (iv) shows the DAP in expanded voltage- and time-scale. Note that LII stellate cells (iv) show a clear sag potential and DAP compared to LII pyramidal cells (iii). **C**, Voltage responses to light stimulation (light blue line) recorded from neurons shown in (A). Average traces (blue) are superimposed on the individual traces (gray). **D-G**, The proportion of responding cells (D), EPSP amplitude (E), the normalized EPSP based on LIII response (F, one-way ANOVA, $F_{3,47} = 33.29$, ***$p < 0.0001$, Bonferroni's multiple comparison test, **$p < 0.01$, ***$p < 0.001$), and the input resistance (G, one-way ANOVA, $F_{3,82} = 21.99$, ***$p < 0.0001$, Bonferroni's multiple comparison test, ***$p < 0.001$) were examined for each cell type (Error bars: mean ± SEM). Abbreviations: LIIs, LII stellate cell; LIIp, LII pyramidal cell.

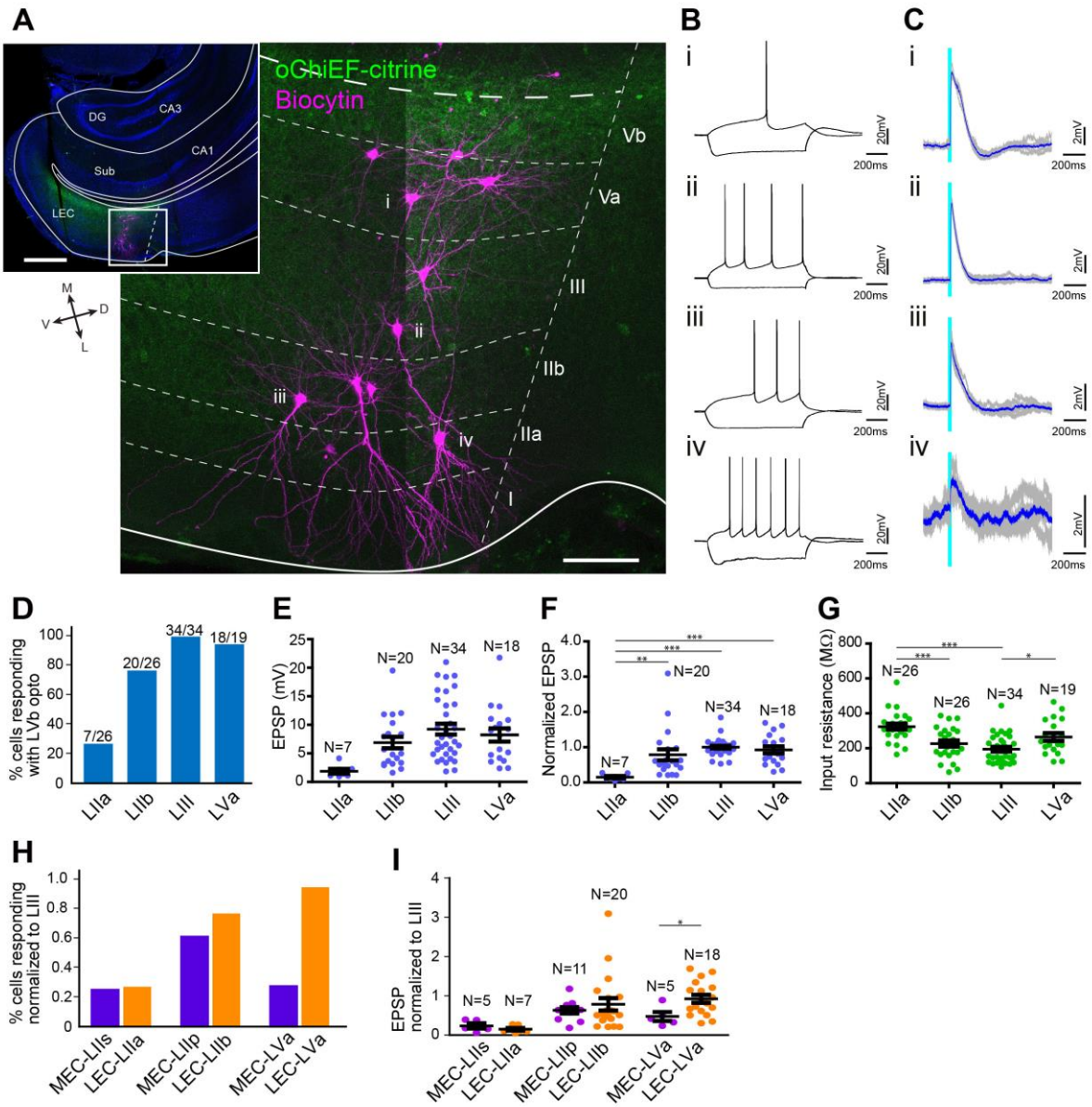

Figure 5. LEC-LVb neurons target LVa pyramidal neurons as well as LII/III pyramidal neurons.

A, Representative image of semicoronal slice showing expression of oChiEF-citrine in LVb neurons (green), and recorded neurons labelled with biocytin (magenta) in LEC. Inset shows a low power image of the section indicating the position of the higher power image. Scale bars represent 500 µm (inset), and 100 µm. **B**, Voltage responses to injected current steps recorded from neurons shown in (A): i, pyramidal cell in LVa; ii, pyramidal cell in LIII; iii, pyramidal cell in LII; iv, fan cell in LII. **C**, Voltage responses to light stimulation (light blue line) recorded from neurons shown in (A). Average traces (blue) are superimposed on the individual traces (gray). **D-G**, The proportion of responding cells (D), EPSP amplitude (E), the normalized EPSP based on LIII response (F, one-way ANOVA, $F_{3,75} = 7.675$, ***p = 0.0002, Bonferroni's multiple comparison test, **$p < 0.01$, ***$p < 0.001$), and the input resistance (G, one-way ANOVA, $F_{3,101} = 11.75$, ***$p < 0.0001$, Bonferroni's multiple comparison test, *$p < 0.05$, ***$p < 0.001$) were examined for each cell type (Error bars: mean ± SEM). **H-I**, Comparison of the proportion of responding cells (H), and the normalized

EPSP based on LIII response (I) between MEC and LEC (Error bars: mean ± SEM; two-tailed unpaired t-test, $t_{21} = 2.239$, $*p = 0.0361$).

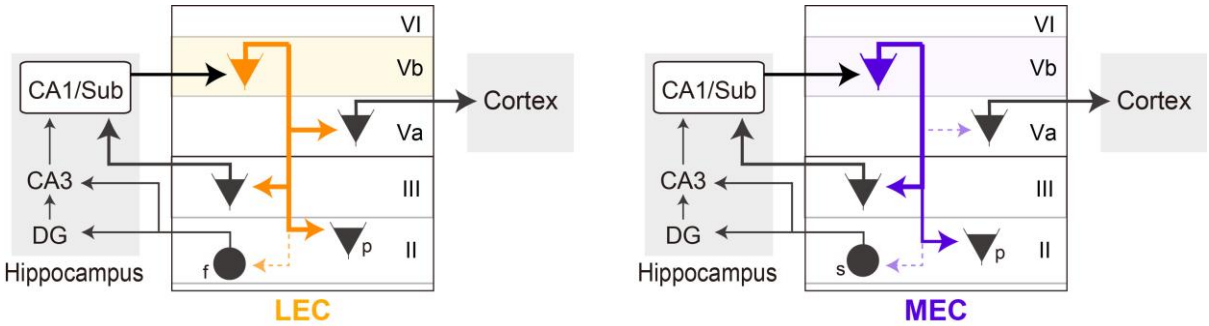

Figure 6. Schematic diagram of the different local circuits in LEC and MEC used by LVb neurons to transfer hippocampal output.

Local connectivity of LVb neurons in LEC (left, orange) and MEC (right, purple). In both LEC and MEC, LVb neurons are the primary recipients of hippocampal output, but the transfer to LVa neurons through direct LVb-to-LVa projections is only present in LEC. Such projections are sparse and weak in MEC. Neurons in LVa are the output neurons of EC, projecting to the neocortex and other telencephalic subcortical structures. In contrast, in both LEC and MEC we find projections from LVb that target pyramidal cells in LIII, including neurons projecting to CA1 and subiculum, and pyramidal cells in LII. Projections to stellate (MEC) and fan (LEC) cells, which project to the dentate gyrus and CA3 are sparse and weak. The output projections of LII pyramidal neurons are not indicated in the figure, they project to ipsilateral-EC, contralateral-EC, CA1, or other telencephalic structures (Ohara et al., 2019). For clarity reasons all these projections are indicated schematically as originating from a single LVb neuron, but this is not yet known. Abbreviations: f, fan cell; s, stellate cell; p, pyramidal cell.